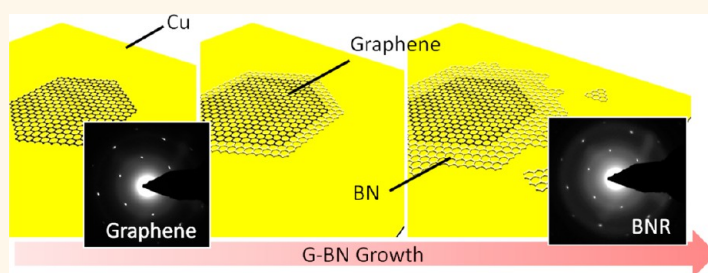


Continuous Growth of Hexagonal Graphene and Boron Nitride In-Plane Heterostructures by Atmospheric Pressure Chemical Vapor Deposition

Gang Hee Han,^{†,§} Julio A. Rodríguez-Manzo,[†] Chan-Woo Lee,[‡] Nicholas J. Kybert,[†] Mitchell B. Lerner,^{†,¶} Zhengqing John Qi,[†] Eric N. Dattoli,[†] Andrew M. Rappe,[‡] Marija Drndic,[†] and A. T. Charlie Johnson^{†,*}

[†]Department of Physics and Astronomy, and [‡]The Makineni Theoretical Laboratories, Department of Chemistry, University of Pennsylvania, Philadelphia, Pennsylvania 19104, United States, and [§]Department of Physics, Sungkyunkwan University (SKKU), Suwon, Korea. [¶]Present address: Functional Nano Devices Laboratory, SPAWAR Naval Systems Center, San Diego, California 92152.

ABSTRACT



Graphene—boron nitride monolayer heterostructures contain adjacent electrically active and insulating regions in a continuous, single-atom thick layer. To date structures were grown at low pressure, resulting in irregular shapes and edge direction, so studies of the graphene—boron nitride interface were restricted to the microscopy of nanodomains. Here we report templated growth of single crystalline hexagonal boron nitride directly from the oriented edge of hexagonal graphene flakes by atmospheric pressure chemical vapor deposition, and physical property measurements that inform the design of in-plane hybrid electronics. Ribbons of boron nitride monolayer were grown from the edge of a graphene template and inherited its crystallographic orientation. The relative sharpness of the interface was tuned through control of growth conditions. Frequent tearing at the graphene—boron nitride interface was observed, so density functional theory was used to determine that the nitrogen-terminated interface was prone to instability during cool down. The electronic functionality of monolayer heterostructures was demonstrated through fabrication of field effect transistors with boron nitride as an in-plane gate dielectric.

KEYWORDS: graphene · boron nitride · heterostructure · chemical vapor deposition · electronic devices

Graphene has been intensively studied as a next-generation electronic material because of its extremely high carrier mobility at room temperature,^{1–4} among other performance advantages. Hexagonal boron nitride (BN) has attracted attention as a two-dimensional, large bandgap dielectric that is chemically and structurally compatible with graphene. This prompted the idea of integrated heterostructures, such as vertical stacking of graphene/BN layers^{5–7} and, more recently, templated growth of one material from the other. In-plane hybrid structures have been generated by lithographical regrowth of BN around patterned graphene⁸

and regrowth of graphene around patterned BN.⁹ In these approaches, the patterning step has the potential to induce unwanted structural and chemical disorder in the resulting hybrid monolayer. To avoid this complication, direct (uninterrupted) growth of in-plane heterostructures has also been investigated, such as few-nanometer scale domains (“patches”) of BN in a graphene matrix¹⁰ and graphene—boron nitride (G-BN) monolayer heterostructures grown on Ru,¹¹ Rh,¹² and Cu¹³ by low pressure chemical vapor deposition (LPCVD). These methods avoided chemical contamination but did not provide control over the interface structure, as discussed in the next paragraph.

* Address correspondence to cjohnson@physics.upenn.edu.

Received for review August 19, 2013 and accepted November 1, 2013.

Published online
10.1021/nn404331f

© XXXX American Chemical Society

Many graphene-enabled device concepts derive functionality from the atomic-scale geometry of the graphene edge.^{14–17} For example, there is significant theoretical interest in lateral G-BN hybrids for use in next-generation digital electronics due to the ability to design devices with energy band modulation.^{18–20} The edge structure of chemical vapor deposition (CVD)-grown graphene is determined by the total chamber pressure and the partial pressure of CH₄ feedstock gas, and typical LPCVD growth of graphene leads to dendritic structures with irregular edges.²¹ In contrast, our experiments were based on atmospheric pressure chemical vapor deposition (APCVD), which promotes the formation of hexagonal graphene flakes with straight, crystallographically aligned edges.^{22–26} We found that precise control of furnace conditions enabled continuous growth of uniform BN ribbons (BNR) from the crystallographically aligned edge of graphene hexagons, where the crystallographic orientation of the BNR was determined by that of graphene seed structure. The most critical factor in the growth of oriented G-BN heterostructures was the use of near-identical, optimized growth conditions for graphene and BN. We found that the growth time could be used to control the width of the BNRs templated by the graphene hexagonal flakes. Isolated BNRs were obtained by annealing the G-BN structure in air at high temperature²⁷ (500 °C, 3 h) to remove the graphene region. We demonstrated that the G-BN interface could be tuned from comparatively sharp to graded by controlling the duration of a preheating period of the BN source. A theoretical analysis of the energetics of the G-BN interface showed that it could be unstable, depending on its atomic termination, a result that was consistent with the observation that the interface was frequently torn. Finally, as a proof-of-concept application, an in-plane side-gated transistor was fabricated based on a graphene channel and side-gate, separated by a BN gate dielectric region, all sharing the same crystallographic orientation. This work paves the way for experiments exploring the properties of nanoscale BNR with well-defined edge structure and known chemical termination.²⁸

RESULTS AND DISCUSSION

APCVD was used instead of LPCVD to obtain hexagonal graphene with straight edges; further, we found that the method could also be used for the controlled growth of triangular BN structures, which to our knowledge has not been previously reported using APCVD. Ammonia borane (AB) was used as the BN feedstock. The direct growth of G-BN structures was enabled by the use of a movable, home-built holder for the AB source. The holder was positioned in a cold zone during the graphene growth phase and then moved to a warm location to initiate sublimation of AB and growth of BN. Details are provided in the Methods

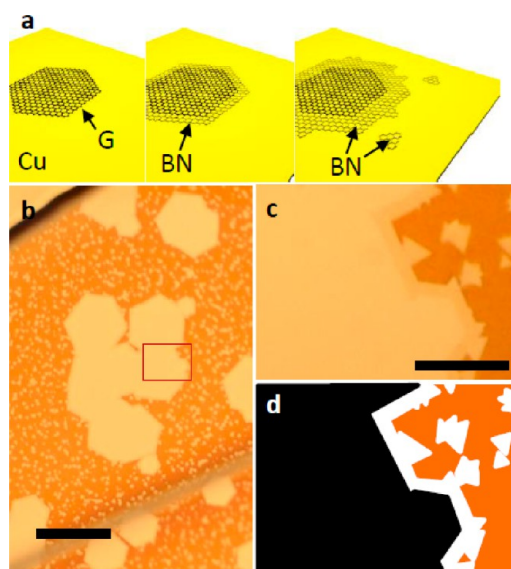


Figure 1. Schematic and optical micrographs of continuous growth of graphene–boron nitride (G-BN) heterostructures. Graphene growth starts from seeds on the Cu foil (a) and hexagonal-BN grows continuously from the graphene template (left to right). (b, c) Low (b) and high (c) magnification image (of region marked with red solid rectangle in panel b) for G-BN heterostructure on the Cu growth substrate that was oxidized by hot plate baking (180 °C, 30 s). In panel c, the graphene flake and BN ribbon and flakes show differing optical contrast. (d) False color black, white, and brown regions indicate graphene, BN, and bare Cu regions in panel c, respectively. Scale bar in panel b is 50 μm , and the scale bar in panel c is 10 μm .

section (Also, see Supplementary Figures 1 and 2 in the Supporting Information).

First, regular graphene hexagons were grown at ca. 1030 °C using CH₄, H₂, and Ar process gases with the AB pellet holder positioned in a cold zone. The AB source was then moved to a position closer to the furnace for a preheating period, during which time the flow of dilute CH₄ feedstock was maintained in order to avoid etching of the hexagonal graphene template by hydrogen (or possibly by impurities present even in ultrahigh purity hydrogen²⁹) while the AB temperature rose to a steady state value of 60–70 °C to induce sublimation.³⁰ It was found that 2 min of preheating led to G-BN structures with a comparatively sharp and straight interface. In contrast, a longer preheating time led to the growth of a graded G-BN interface due to coinjection of CH₄ and AB feedstock. After the preheating period, the CH₄ gas flow was stopped, and there was a BN growth phase that lasted 2–10 min, followed by rapid sample cooling.

Figure 1a is a schematic of the growth progression for G-BN hybrid monolayers, as inferred from the result of multiple growth runs (see Supplementary Figure 3 and inset to Supplementary Figure 7 of the Supporting Information). During the graphene growth period, regular hexagonal structures nucleated and grew (left, Figure 1a), and their shape was preserved during the AB source preheating period. For the first few minutes, BN grew exclusively as nanoribbons aligned

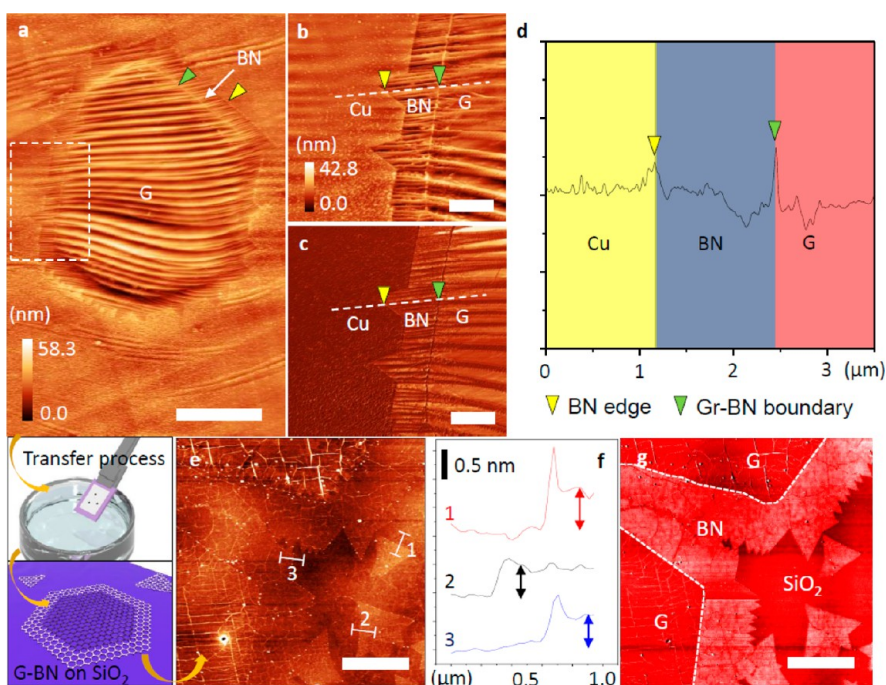


Figure 2. Atomic force microscopy (AFM) analysis of G-BN heterostructures on Cu growth substrate and after transfer to a silicon dioxide surface (a–d) AFM images and line scans of G-BN heterostructure on Cu and (e–g) after transfer onto an oxidized silicon wafer. In panels a–d, topographical AFM images were taken after the sample was baked at 180 °C for 1 min. Yellow and green triangles indicate the BN edge and G-BN boundary, respectively. (a) Low-magnification image of G-BN flake; (b) higher magnification topographic; and (c) phase image from the dashed rectangle in panel a; (d) height profiles of bare Cu–BN–G; (e) topographical image of G-BN on SiO₂ (300 nm oxide)/Si wafer, and (f) height profiles (1–3) in panel e; (g) phase-mode image shows the G-BN boundary clearly. Scale bars in panels a, e, and g are 4 μm. Scale bars in panels b and c are 1 μm.

along the edges of the graphene hexagons (middle, Figure 1a), while isolated triangular flakes of BN nucleated and grew at later times (right, Figure 1a). We concluded that the edges of the graphene hexagons are more reactive for BN growth than bare Cu foil. Figure 1b is an optical micrograph that shows G-BN hybrid structures and triangular BN flakes on Cu foil. To create the optical contrast, the sample was oxidized for 30–60 s on a hot plate at 180 °C after the growth. The morphology of the BNRs along the edge of the graphene hexagon is clearly seen at higher magnification (Figure 1c,d; Figure 1d is a false color version of the image in Figure 1c). Further details of the growth of BN ribbons from graphene templates can be found in Supplementary Figure 3 of the Supporting Information).

Figure 2a is a topographic image of the sample taken by atomic force microscopy (AFM) after Cu oxidation. Both the graphene and BN regions show wrinkles, assumed to arise from differential thermal expansion of the material compared to the copper growth substrate. Oxidation led to volume expansion of the Cu foil, so the oxidized Cu surface was observed to be slightly higher than the edge of BN (Figure 2a–d; yellow and green triangles indicate the transition from BN to oxidized Cu and the G-BN interface, respectively). These images provided strong evidence that BNRs grew directly from graphene edge atoms, and not by stitching of seeds that grew on the Cu foil. First, as noted previously, BNR formation occurred during the

first 3 min of growth, while BN triangle flakes grew at later times from seeds on the Cu foil. This time lag suggested a distinctly different growth mechanism for the two structures. Second, the observation of straight G-BN interfaces (Figure 2b,c) provided strong support for the direct growth of BN from the hexagonal graphene template.

To establish the monolayer nature of G-BN heterostructures, we transferred the sample to Si/SiO₂ wafers by the bubbling transfer technique.²⁶ The height profile of the G-BN (Figure 2e) shows that the structure is ~0.5 nm in height, consistent with a single atomic layer, and that there is no significant height difference between the graphene and BN regions. However, the materials are clearly distinguishable in the phase image, consistent with earlier observations.⁸

Raman spectroscopy may be used to identify both graphene and BN, although the BN signal is weak compared to that of graphene.³¹ This technique was used to establish the presence of both graphene and BN in hybrid structures that had been transferred onto oxidized silicon substrates. Because of the proximity of the strong D peak of graphene (1360 cm⁻¹) to the much weaker characteristic peak of BN (1373 cm⁻¹), it was not possible to collect signals from both materials simultaneously. Instead, we first collected a Raman line map that established the presence of the graphene hexagon (Figure 3a, top). The sample was then oxidized at 500 °C in air for 3 h to remove the graphene

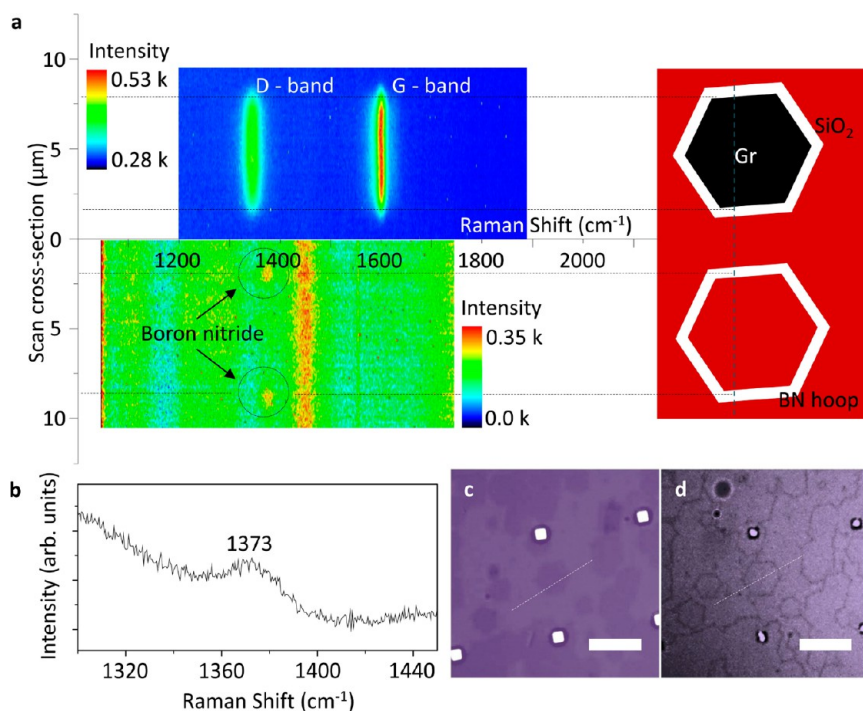


Figure 3. 1D Raman maps of G-BN and BN structures. (a) 1d Raman spectrum map across G-BN (top) and BN ribbons (BNR, bottom) after graphene removal by heat treatment (500 °C, 3 h) in air; (b) Raman spectrum of the BNR showing the characteristic peak of BN centered near 1373 cm^{-1} . (c, d) Optical micrographs before (c) and after (d) the heat treatment used to remove graphene. Contrast and gamma values of panel d were modified to enhance the visibility of the BN nanoribbons on the substrate. Scale bars are 10 μm .

(Supplementary Figure 4 of the Supporting Information), and a second Raman map along the same line showed that BNRs remained in the regions that were along the two opposite sides of the graphene hexagon (Raman peaks near 1370 cm^{-1} indicated by circles in Figure 3a, bottom). Figure 3b shows the corresponding Raman spectrum collected in one of the circled regions. The full spectrum of the graphene and BN ribbon is provided in Supplementary Figure 5 of the Supporting Information. The presence of the Gr hexagon and BN ribbon was also inferred from optical micrographs taken before and after the oxidation step (Figure 3c,d).

We further characterized G-BN heterostructures by electron energy loss spectroscopy (EELS) in a transmission electron microscope (TEM). For TEM analysis, G-BN samples were transferred onto amorphous carbon TEM grids with 1 μm holes (Figure 4a). Energy-filtered images (Figure 4a, inset) conclusively showed the presence of B and N only in the region identified as the BNR. The presence of B and N at such regions was confirmed by EELS (see Supplementary Figure 6a of the Supporting Information) spectra that showed the K-edge peaks for B and N (188 and 400 eV, respectively); a weak carbon peak was also observed at 283 eV due to the carbon deposition during transfer, as observed by others.^{30,32,33}

Electron diffraction (ED) analysis of hexagonal graphene flakes, covering areas of 16 μm^2 (Supplementary Figure 6b of the Supporting Information), showed that

the majority had a single crystal orientation with zigzag edges. Strikingly, the crystal orientation of the BNR consistently matched that of the graphene template from which they grew. This is shown in Figure 4b, where a dark-field (DF) TEM image taken with only one diffracted beam fixed at an angle corresponding to an atomic plane spacing of 0.12 nm highlights the continuity of the crystal orientation across the interface of the G-BN structure. Figure 4c shows ED patterns taken from the areas labeled as i (G), ii (BN), iii (G-BN), and iv (G) in Figure 4b. The crystallographic orientations were identical to within 2 degrees. Larger deviations (~ 5 degree) in the orientations of G-BN were also observed near torn or folded regions, usually at the interface.

Although theoretical predictions of favorable electronic properties (*e.g.*, half metallicity³⁴ and bandgap modulation^{18–20,34}) have motivated the synthesis of G-BN hybrid structures, to date less attention has been paid to their structural stability, which is a prerequisite in order to access their desirable electrical properties. Strikingly, we observed frequent tearing at the G-BN interface, even in the absence of postsynthesis treatment or handling (*e.g.*, sample baking or transfer process; see Supplementary Figure 7 of the Supporting Information). From this we concluded that the G-BN interface was vulnerable to fracture by thermal stress associated with the cooling process. To support this conjecture, we investigated the thermodynamics of G-BN interfaces from first principles to analyze the

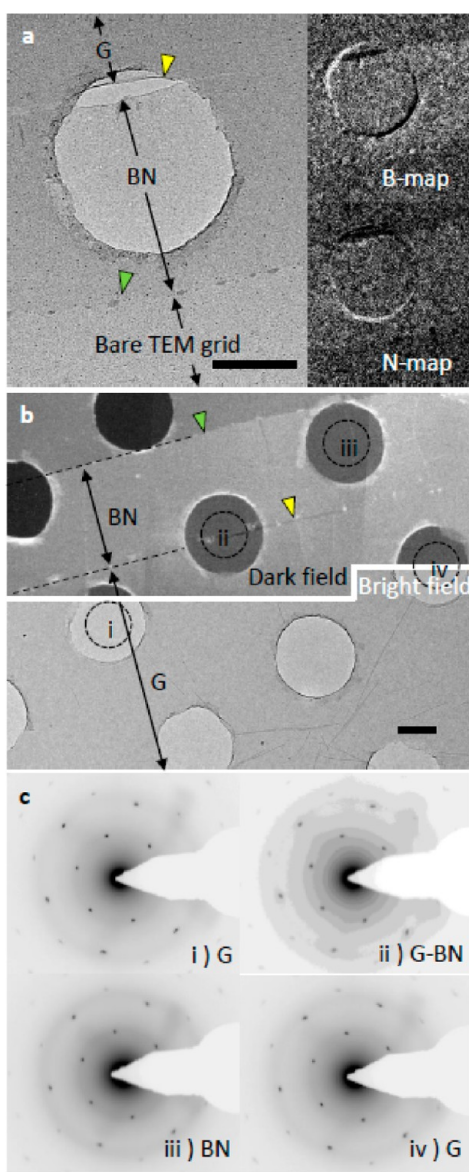


Figure 4. Transmission electron microscopy (TEM) and electron diffraction (ED) analysis. (a) TEM image of a region containing both a G-BN boundary (yellow arrow) and a BN ribbon with its termination (green arrow). Scale bar is 400 nm. Inset: Energy filtered images for B and N, proving that BN is present only in the ribbon region. (b) Composite dark-field (top)/bright-field (bottom)-TEM image and ED data confirming that the graphene and BN regions have the same crystallographic orientation (see text). (c) ED patterns were taken from the areas labeled as i, ii, iii, and iv in panel b (each diffraction pattern was taken from a $0.6 \mu\text{m}$ diameter area).

relevant energetics. Specifically, density functional theory (DFT) total energy calculations of graphene, BN, and hybrids were performed and compared (Figure 5a). Since graphene hexagonal flakes are known to have a zigzag edge structure,^{22–26} we considered two interface structures, one terminated by boron and the other by nitrogen (Figure 5b). To incorporate the influence of hydrogen gas at high temperature, we used first-principles thermodynamics:

the tearing free energy was defined as

$$G_{\text{tearing}} = G_{\text{BN}} + G_{\text{GR}} - \left(G_{\text{GR-BN}} + \frac{1}{2} n_{\text{H}} \mu_{\text{H}_2} \right)$$

where n_{H} is the number of H atoms that saturate dangling bonds after tearing and μ_{H_2} is the chemical potential of H_2 at temperature T and pressure P . The temperature range used was typical of the postsynthesis cooling process (see the Materials and Methods section for further details of the calculation). The G-BN interfaces for both B and N terminations were found to be less stable than lines of bonds within either graphene or BN. Furthermore, the B termination was calculated to be more stable than the N termination. The computed first-principles thermodynamics predicted that the N-terminated G-BN interface is less stable than separated, hydrogenated graphene and BN for $T < 600$ K.

The instability of the N-terminated interface can be explained as a result of hybridization and charge transfer. The electronic configurations of B and N are $1s^2 2s^2 2p^1$ and $1s^2 2s^2 2p^3$, respectively. To become iso-electronic with graphene, both atoms hybridize as sp^2 , and electrons transfer from N to B. Accordingly, the bonding character of BN is relatively ionic, in contrast to that of graphene, which is completely covalent. For the B-terminated G-BN interface, carbon at the edge of graphene is predicted to donate electrons to B, filling π -bonding states (Figure 5b, left side). In contrast, the N-terminated structure requires charge transfer from N to C, which results in the occupation of antibonding states (Figure 5b, right side) and weaker interfacial bonding. These contrasting bonding motifs explain the difference in net tearing free-energy for the two terminations, and lead to the conclusion that the N-terminated interface would be vulnerable to spontaneous separation during cooling.

We found that extending the duration of the preheating period of the AB source material enabled the generation of a G-BN interface that was graded on the micrometer scale. This was demonstrated in experiments where G-BN heterostructures were grown with 0, 2, 4, and 6 min of AB preheating. It was found that 2 min was the optimal choice for generation of a comparatively sharp G-BN interface. For 0 and 2 min of preheating, the graphene Raman signal was uniform over the entire flake (in Figure 3a, top), which was interpreted to imply that there was no significant etching of the graphene template by hydrogen gas (or associated impurities²⁹), and that no B or N impurity atoms were incorporated into the bulk of the graphene flake. In contrast, for samples grown with a longer preheating period, the intensity of the D- and D'-bands (indicative of disorder) increased progressively near the G-BN interface, while the G-band intensity associated with C–C bonding decreased (Figure 6a, b). This was attributed to incorporation of boron and/or nitrogen impurity atoms in the graphene region, similar to

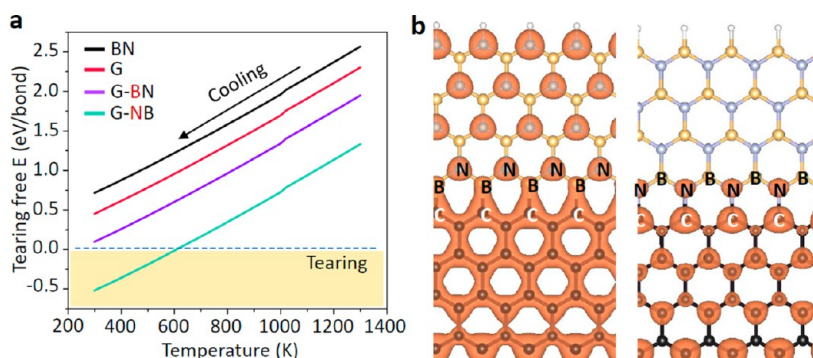


Figure 5. DFT calculations of G-BN and related structures. (a) Calculated dependence of tearing energy versus temperature with $p(\text{H}_2) = 0.01$ atm. Black, red, purple, and light blue curves indicate tearing energies of BN, graphene, B-terminated G-BN, and N-terminated G-BN, respectively. (b) Real-space charge density of G-BN. N-terminated G-BN (right) is predicted to be weaker than B-terminated G-BN (left) due to the presence of filled antibonding interfacial states.

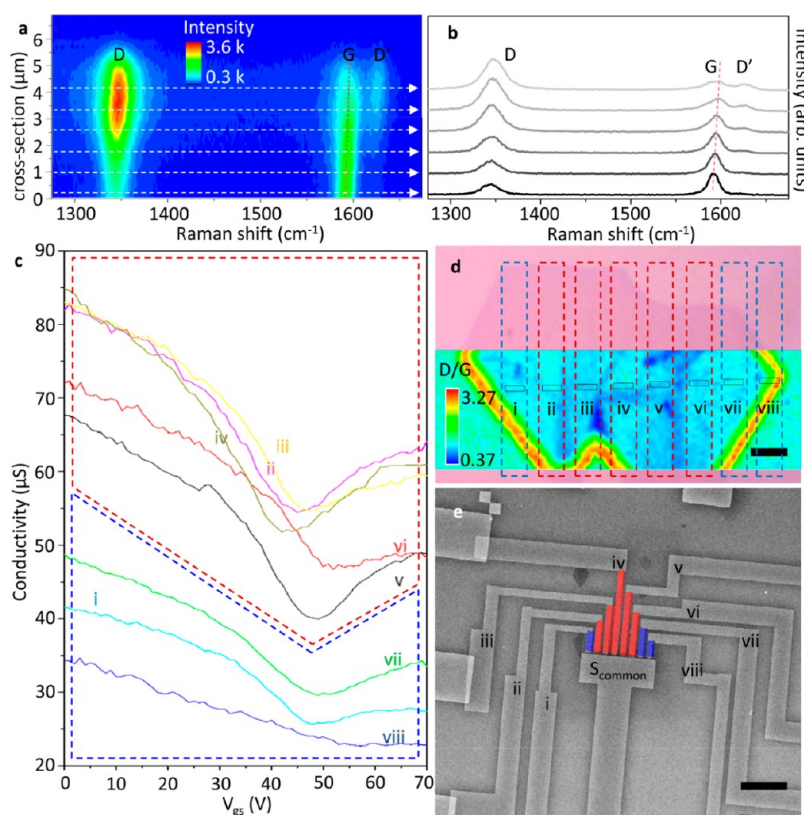


Figure 6. Influence of ammonia borane (AB) preannealing time on G-BN growth (a,b). (a) 1-D Raman map from a G-BN sample grown using a 6 min preanneal of the AB source. (b) Raman spectra from the six locations indicated by white dashed lines in panel a. (c–e) $I-V_g$ measurements were taken from the edge (blue dashed line, i, vii, viii) and middle (red dashed line, ii–vi) of the G-BN flake: (c) $I-V_g$ data from the selected area in panel d. (d) Optical image and 2-D Raman mapping (D/G) for the device. Solid boxes are the device channels. Scale bar, 4 μm. (e) Scanning electron micrograph of the device. The source (S) was fabricated as a common electrode. Scale bar, 20 μm.

what has been reported for *h*-BNC film growth.¹⁰ To support this interpretation, a multielectrode, back-gated device was fabricated to enable electrical measurements of specified regions within the graphene flake. Conductivity and carrier mobility decreased progressively for regions nearer to the G-BN interface, consistent with the formation of a graded interface where the carbon component decreased monotonically toward the G-BN interface (Figure 6c).

Unzipping of boron nitride nanotubes^{35–37} by Ar⁺ ion bombardment is one approach to obtain BN nanoribbons for use in electronics. On the basis of the results presented in Figure 3, it was clear that an alternative approach is the use of single-crystal graphene as a sacrificial template for BNR growth. This motivated a study of methods to control the BNR width and in this way to enable bottom-up BN nanoribbon synthesis. To this end, we first reduced the BN growth

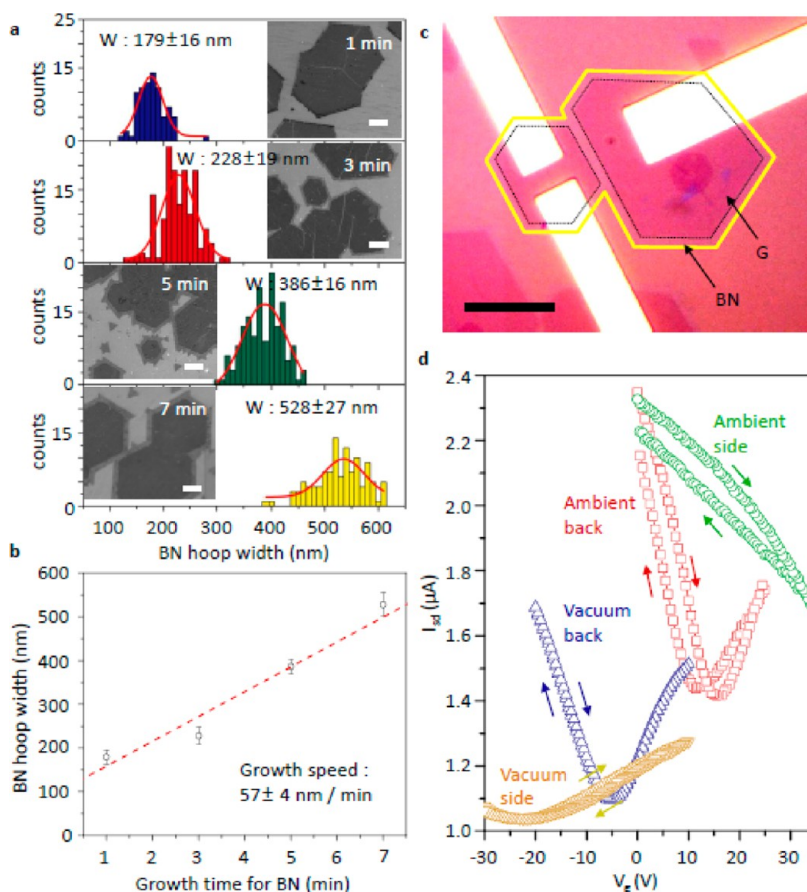


Figure 7. Width control of boron nitride ribbon around graphene flake; BN width around graphene controlled by growth time. (a) For 1–6 (top–bottom) the min growth time, 6 min, was used for preannealing. (b) Extracted growth rate is 57 ± 4 nm/min. (c) Two graphene flakes (edges indicated by dashed black lines) are separated by a boron nitride gate dielectric region (edge shown by a solid yellow line). Scale bar is $10 \mu\text{m}$. (d) I – V characteristics for the device in panel c.

temperature to $1000 \text{ }^\circ\text{C}$ to reduce the BN growth rate. We determined that at this temperature, the optimum preannealing period of the AB source was increased to 6 min, compared to 2 min for a growth temperature of $1030 \text{ }^\circ\text{C}$. G-BN heterostructures were grown using BN growth times of 1–7 min (see Figure 7a), and the corresponding widths of the BNRs were 179 ± 16 , 228 ± 19 , 386 ± 16 , and 528 ± 27 nm, respectively, for a growth rate of 57 ± 4 nm/min (Figure 7b). For growth times less than 1 min, we expect that BN nanoribbons of a few tens of nanometers in width could be reproducibly obtained.

Synthesis of high quality in-plane G-BN heterostructures marks a critical step toward the realization of “2D electronics.”^{8,9} As a proof-of-concept of the electronic functionality of the hybrid structures, we fabricated three-terminal, side-gated devices^{38–40} on oxidized silicon substrates, where BN served as the gate insulator. To accomplish this, G-BN flakes were transferred onto 300 nm of a SiO_2/Si wafer, and graphene flakes were identified that were crystallographically aligned and where the region between the flakes was filled by BN (Figure 7c). One flake was contacted by two electrodes that served as a source and drain, while the

other flake was contacted by a third electrode to serve as a side-gate. This is seen in Figure 7c, where black dashed and yellow solid lines indicate the boundaries between G-BN and BN-bare SiO_2 , respectively. The I_{ds} – V_g characteristics of the device were measured using the global back gate and the side gate in ambient and under a vacuum of 1×10^{-6} Torr (Figure 7d). The red (square) data set in Figure 7d, recorded in ambient, has a Dirac point near 15 V, which is typical for a back-gated graphene device that is *p*-doped by atmospheric impurities. The transconductance associated with the side gate was about five times smaller than that of the back-gate under both ambient and vacuum conditions, consistent with estimates of the geometric capacitances of these two configurations. In vacuum, the charge neutrality point for the back gate was -5 V, which was consistent with electrode doping.⁴¹ The side gate data in vacuum (yellow inverted triangle) had a more negative Dirac point (-22 V), as expected since its geometric capacitance was about five times smaller than that of the back gate.

CONCLUSIONS

G-BN heterostructure monolayers were grown *via* APCVD, which is advantageous for obtaining graphene

templates with well-defined edge structures. We demonstrated that precise control of the furnace conditions enabled continuous growth of regular BNR with the same crystallographic orientation as the graphene growth template, as evidenced by AFM, TEM, and electron diffraction measurements. The preheating time of the BN source was found to be a critical parameter that could be used to create either a sharp or graded G-BN interface. We also studied tearing at the G-BN interface, which was often observed, presumably due to strain induced during the cooling

process. DFT calculations demonstrated that the N termination is weaker than the B termination due to the presence of the antibonding state occupation, although, both B and N termination were found to be energetically possible. We also quantified the growth rate of the BNRs and demonstrated the electronic functionality of G-BN heterostructures where the BN region was used as an in-plane gate dielectric. Our approach may open up a route for the growth of BNR of nanoscale dimensions and pave the way for 2D G-BN hybrid electronics.

MATERIALS AND METHODS

Graphene–Boron Nitride Heterostructure Growth. Graphene–boron nitride (G-BN) lateral heterostructure monolayers were synthesized by introducing diluted CH_4 (GTS-WELCO, 1.05%, balanced by Ar) and ammonia borane (AB) source (Sigma-Aldrich, 682098) into a 1 in. tube furnace. The AB source was prepared according to the procedure in Supplementary Figure 1 of the Supporting Information. A 100 μm thick Cu foil (Alfa Aesar, 42189), either polished^{42,43} or unpolished, was loaded into the tube furnace (Lindberg blue M, TF55035) and heated to 1057 °C for 25 min in a flow of 500 sccm of Ar (99.999%) and 50 sccm of H_2 (99.999%). After 5 min of annealing, the system was cooled to 1030 °C (1000 °C for Figure 7a and 7b to reduce growth rate) for 5 min to grow hexagonal graphene flakes. The process gas flows were 500 sccm of Ar, 30–35 sccm H_2 , and 2 sccm of diluted (1.02% in Ar) CH_4 . Graphene was grown for 8–20 min then the AB source was moved closer to the furnace (Supplementary Figure 2c of the Supporting Information). The AB source was preannealed for 2 min or longer (e.g., 6 min for flake in Figure 6) to induce sublimation, while H_2 and CH_4 gas flows were continued to prevent etching of graphene. After the preannealing step, H_2 gas flow was reduced to 20 sccm, the CH_4 gas flow was stopped, and sublimed material from the AB pellet was used to grow hoop-like BNR around the graphene templates for 1 to 7 min. When the BN growth finished, the furnace was rapidly cooled to the room temperature in a flow of 1000 sccm of Ar and 10 sccm of H_2 .

Sample Characterization by AFM, TEM, SEM, and Raman Spectroscopy. AFM (Asylum, MFP-3D) images of G-BN heterostructures on Cu foil and SiO_2/Si (300 nm oxide) were taken with tapping mode. For TEM analysis, the sample was transferred to a holey (1 μm hole) carbon grid (Electron Microscopy Sciences, c-flat) by bubbling transfer method²⁶ with poly(methyl-methacrylate) (Microchem, molecular weight of 950 K). Transmission electron microscopy, electron diffraction, and electron energy loss spectroscopy (EELS) were carried out in a JEOL 2010, a JEOL 2010F, and a FEI Titan operating at 200, 200, and 300 kV, respectively. Electron energy loss (EEL) spectra and energy filtered TEM images were acquired with a GIF camera. In particular, filtered images were taken with 30 eV energy windows centered at 188 and 401 eV, for B and N, respectively. Scanning electron microscopy images were taken with 5 kv operation bias. For Raman spectroscopy and mapping, the G-BN flake was transferred onto an oxidized silicon wafer and Raman measurements were taken using an excitation laser with a wavelength of 532 nm wavelength.

DFT Calculation. DFT calculations were performed using Quantum ESPRESSO⁴⁴ with generalized gradient approximation (GGA-PBE)⁴⁵ for exchange-correlation functionals. Norm-conserving nonlocal pseudopotentials within the Rappe-Rabe-Kaxiras-Joannopoulos (RRKJ)^{46,47} scheme were adopted to generate plane-wave pseudopotentials of B, C, N, and H atoms. The basis set kinetic energy cutoff was 50 Ry. Convergence thresholds for self-consistency and ionic relaxation were set as 1×10^{-6} Ry and 1×10^{-3} Ry/Bohr, respectively. Monkhorst-Pack⁴⁸ k-point meshes $3 \times 1 \times 1$ were used for supercells consisting of 32 hexagons with eight zigzag chains (eight atoms per chain). The tearing free energy was calculated with an

assumption that tearing is achieved with zigzag terminations for pristine BN and GR, and their hybrid. The model sheets were separated by a vacuum region of 10 Å, and their edges are saturated by hydrogen atoms.

Conflict of Interest: The authors declare no competing financial interest.

Acknowledgment. This work was supported by the Nano/Bio Interface Center through the National Science Foundation NSEC DMR08-32802 and ENG-1312202. G.H.H. was supported by the Postdoctoral Research Program of Sungkyunkwan University, 2011 (SKKU). J.A.R.M. and M.D. were supported by NIH grant R21HG006313. C.-W. L. was supported by the Department of Energy Office of Basic Energy Sciences, under Grant No. DE-FG02-07ER15920. A.M.R. was supported by the Air Force Office of Scientific Research, Air Force Materiel Command, USAF, under Grant FA9550-10-1-0248. Electron Microscopy was carried out (in part) at the Center for Functional Nanomaterials, Brookhaven National Laboratory, which is supported by the U.S. Department of Energy, Office of Basic Energy Sciences, under Contract No. DE-AC02-98CH10886. The authors acknowledge use of facilities associated with the Nano/Bio Interface Center (Raman spectroscopy, AFM) and the Nanoscale Characterization Facility (TEM) at the University of Pennsylvania.

Supporting Information Available: Preparation of the ammonia-borane (AB) source pellet. Diagram and description of the home-built sliding holder for the AB source. Additional data on the growth of boron nitride from graphene observed by optical microscopy. Atomic force microscopy image of annealed Gr-BN layer. Raman spectrum of oxidized silicon substrate compared to that of the same substrate with transferred BN material. Electron energy loss spectrum from boron nitride ribbon and electron diffraction data from graphene showing the lack of detectable grain boundaries. Scanning electron micrograph of tearing at the Gr–BN interface induced by sample cooling. This material is available free of charge via the Internet at <http://pubs.acs.org>.

REFERENCES AND NOTES

- Novoselov, K. S.; Geim, A. K.; Morozov, S. V.; Jiang, D.; Zhang, Y.; Dubonos, S. V.; Grigorieva, I. V.; Firsov, A. A. Electric Field Effect in Atomically Thin Carbon Films. *Science* **2004**, *306*, 666–669.
- Zhang, Y.; Tan, Y.-W.; Stormer, H. L.; Kim, P. Experimental Observation of the Quantum Hall Effect and Berry's Phase in Graphene. *Nature* **2005**, *438*, 201–204.
- Bolotin, K. I.; Sikes, K. J.; Jiang, Z.; Klima, M.; Fudenberg, G.; Hone, J.; Kim, P.; Stormer, H. L. Ultrahigh Electron Mobility in Suspended Graphene. *Solid State Commun.* **2008**, *146*, 351–355.
- Chen, J. H.; Jang, C.; Xiao, S. D.; Ishigami, M.; Fuhrer, M. S. Intrinsic and Extrinsic Performance Limits of Graphene Devices on SiO_2 . *Nat. Nanotechnol.* **2008**, *3*, 206–209.
- Britnell, L.; Gorbachev, R. V.; Jalil, R.; Belle, B. D.; Schedin, F.; Mishchenko, A.; Georgiou, T.; Katsnelson, M. I.; Eaves, L.; Morozov, S. V.; et al. Field-Effect Tunneling Transistor

- Based on Vertical Graphene Heterostructures. *Science* **2012**, *335*, 947–950.
- Dean, C. R.; Young, A. F.; Meric, I.; Lee, C.; Wang, L.; Sorgenfrei, S.; Watanabe, K.; Taniguchi, T.; Kim, P.; Shepard, K. L.; et al. Boron Nitride Substrates for High Quality Graphene Electronics. *Nat. Nanotechnol.* **2010**, *5*, 722–726.
 - Quhe, R.; Zheng, J.; Luo, G. L.; Liu, Q.; Qin, R.; Zhou, J. N.; Yu, D.; Nagase, S.; Mei, W.-N.; Gao, Z.; et al. Tunable and Sizable Band Gap of Single-Layer Graphene Sandwiched between Hexagonal Boron Nitride. *NPG Asia Mater.* **2012**, *4*, e6.
 - Levendorf, M. P.; Kim, C.-J.; Brown, L.; Pinshane, Y. H.; Havener, R. W.; Muller, D. A.; Park, J. Graphene and Boron Nitride Lateral Heterostructure for Atomically Thin Circuitry. *Nature* **2012**, *488*, 627–632.
 - Liu, Z.; Ma, L.; Shi, G.; Zhou, W.; Gong, Y.; Lei, S.; Yang, X.; Zhang, J.; Yu, J.; Hackenberg, K. P.; et al. In-Plane Heterostructures of Graphene and Hexagonal Boron Nitride with Controlled Domain Sizes. *Nat. Nanotechnol.* **2013**, *8*, 119–124.
 - Ci, L.; Song, L.; Jin, C.; Jariwala, D.; Wu, D.; Li, Y.; Srivastava, A.; Wang, Z. F.; Storr, K.; Balicas, L.; et al. Atomic Layers of Hybridized Boron Nitride and Graphene Domains. *Nat. Mater.* **2010**, *9*, 430–435.
 - Sutter, P.; Cortes, R.; Lahiri, J.; Sutter, E. Interface Formation in Monolayer Graphene–Boron Nitride Heterostructures. *Nano Lett.* **2012**, *12*, 4869–4874.
 - Gao, Y.; Zhang, Y.; Chen, P.; Li, Y.; Liu, M.; Gao, T.; Ma, D.; Chen, Y.; Cheng, Z.; Qiu, X.; et al. Toward Single-Layer Uniform Hexagonal Boron Nitride-Graphene Patchworks with Zigzag Linking Edges. *Nano Lett.* **2013**, *13*, 3439–3443.
 - Kim, S. M.; Hsu, A. L.; Araujo, P. T.; Lee, Y.-H.; Palacios, T.; Dresselhaus, M.; Idrobo, J.-C.; Kim, K. K.; Kong, J. Synthesis of Patched or Stacked Graphene and HBN Flakes: A Route to Hybrid Structure Discovery. *Nano Lett.* **2013**, *13*, 933–941.
 - Fujita, M.; Wakabayashi, K.; Nakada, K.; Kusakabe, K. Peculiar Localized State at Zigzag Graphite Edge. *J. Phys. Soc. Jpn.* **1996**, *65*, 1920.
 - Nakada, K.; Fujita, M.; Dresselhaus, G.; Dresselhaus, M. S. Edge State in Graphene Ribbons: Nanometer Size Effect and Edge Shape Dependence. *Phys. Rev. B* **1996**, *54*, 17954–17961.
 - Ritter, K. A.; Lyding, J. W. The Influence of Edge Structure on the Electronic Properties of Graphene Quantum Dots and Nanoribbons. *Nat. Mater.* **2009**, *8*, 235–242.
 - Liu, Y.; Dobrinsky, A.; Yakobson, B. I. Graphene Edge from Armchair to Zigzag: The Origins of Nanotube Chirality? *Phys. Rev. Lett.* **2010**, *105*, 235502.
 - Zhang, A.; Teoh, H. F.; Dai, Z. H.; Feng, Y. P.; Zhang, C. Band Gap Engineering in Graphene and Hexagonal BN Antidot Lattices: A First Principles Study. *Appl. Phys. Lett.* **2011**, *98*, 023105.
 - Fiori, G.; Betti, A.; Bruzzone, S.; Iannaccone, G. Lateral Graphene-HBCN Heterostructures as a Platform for Fully Two-Dimensional Transistors. *ACS Nano* **2012**, *6*, 2642–2648.
 - Fan, X.; Shen, Z.; Liu, A. Q.; Kuo, J.-L. Band Gap Opening of Graphene by Doping Small Boron Nitride Domains. *Nanoscale* **2012**, *4*, 2157–2165.
 - Li, X.; Magnuson, C. W.; Venugopal, A.; Tromp, R. M.; Hannon, J. B.; Vogel, E. M.; Colombo, L.; Ruoff, R. S. Large-Area Graphene Single Crystals Grown by Low-Pressure Chemical Vapor Deposition of Methane on Copper. *J. Am. Chem. Soc.* **2011**, *133*, 2816–2819.
 - Luo, Z.; Kim, S.; Kawamoto, N.; Rappe, A. M.; Johnson, A. T. C. Growth of Hexagonal Shape Graphene Flakes with Zigzag Edges. *ACS Nano* **2011**, *11*, 9154–9160.
 - Vlassioug, I.; Regmi, M.; Fulvio, P.; Dai, S.; Datskos, P.; Eres, G.; Smirnov, S. Role of Hydrogen in Chemical Vapor Deposition Growth of Large Single-Crystal Graphene. *ACS Nano* **2011**, *5*, 6069–6076.
 - Wu, B.; Geng, D.; Guo, Y.; Huang, L. M.; Xue, Y.; Zheng, J.; Chen, J.; Liu, Y.; Jiang, L.; Hu, W. Equiangular Hexagon-Shape-Controlled Synthesis of Graphene on Copper Surface. *Adv. Mater.* **2011**, *23*, 3522–3525.
 - Yu, Q.; Jauregui, L. A.; Wu, W.; Colby, R.; Tian, J.; Su, Z.; Cao, H.; Liu, Z.; Pandey, D.; Wei, D.; et al. Control and Characterization of Individual Grains and Grain Boundaries in Graphene Grown by Chemical Vapor Deposition. *Nat. Mater.* **2011**, *10*, 443–449.
 - Gao, L.; Ren, W.; Xu, H.; Jin, L.; Wang, Z.; Ma, T.; Ma, L.-P.; Zhang, Z. T.; Fu, Q.; Peng, L.-M.; et al. Repeated Growth and Bubbling Transfer of Graphene with Millimetre-Size Single Crystal Grains Using Platinum. *Nat. Commun.* **2012**, *3*, 699.
 - García, A. G. F.; Neumann, M.; Amet, F.; Williams, J. R.; Watanabe, K.; Taniguchi, T.; Goldhaber-Gordon, D. Effective Cleaning of Hexagonal Boron Nitride for Graphene Devices. *Nano Lett.* **2012**, *12*, 4449–4454.
 - Lopez-Bezanilla, A.; Huang, J.; Terrones, H.; Sumpter, B. G. Boron Nitride Nanoribbons Become Metallic. *Nano Lett.* **2011**, *11*, 3267–3273.
 - Choubak, S.; Biron, M.; Levesque, P. L.; Martel, R.; Desjardins, P. No Graphene Etching in Purified Hydrogen. *J. Phys. Chem. Lett.* **2013**, *4*, 1100–1103.
 - Kim, K. K.; Hsu, A. L.; Jia, X.; Kim, S. M.; Shi, Y.; Hofmann, M.; Nezich, D.; Rodriguez-Nieva, J. F.; Dresselhaus, M.; Palacios, T.; et al. Synthesis of Monolayer Hexagonal Boron Nitride on Cu Foil Using Chemical Vapor Deposition. *Nano Lett.* **2012**, *12*, 161–166.
 - Gorbachev, R. V.; Riaz, I.; Nair, R. R.; Jalil, R.; Britnell, L.; Belle, B. D.; Hill, E. W.; Novoselov, K. S.; Watanabe, K.; Taniguchi, T.; et al. Hunting for Monolayer Boron Nitride: Optical and Raman Signatures. *Small* **2011**, *7*, 465–468.
 - Lee, K. H.; Shin, H.-J.; Lee, J.; Lee, I.-y.; Kim, G.-H.; Choi, J.-Y.; Kim, S.-W. Large-Scale Synthesis of High-Quality Hexagonal Boron Nitride Nanosheets for Large-Area Graphene Electronics. *Nano Lett.* **2012**, *12*, 714–718.
 - Song, L.; Ci, L.; Lu, H.; Sorokin, P. B.; Jin, C.; Ni, J.; Kvashnin, A. G.; Kvashnin, D. G.; Lou, J.; Yakobson, B. I.; et al. Large Scale Growth and Characterization of Atomic Hexagonal Boron Nitride Layers. *Nano Lett.* **2010**, *10*, 3209–3215.
 - Liu, Y.; Wu, X.; Zhao, Y.; Zeng, X. C.; Yang, J. Half-Metallicity in Hybrid Graphene/Boron Nitride Nanoribbons with Dihydrogenated Edges. *J. Phys. Chem. C* **2011**, *115*, 9442–9450.
 - Zeng, H.; Zhi, C.; Zhang, Z.; Wei, X.; Wang, X.; Guo, W.; Bando, Y.; Golberg, D. “White Graphenes”: Boron Nitride Nanoribbons Via Boron Nitride Nanotube Unwrapping. *Nano Lett.* **2010**, *10*, 5049–5055.
 - Erickson, K. J.; Gibb, A. L.; Sinitzskii, A.; Rouseas, M.; Alem, N.; Tour, J. M.; Zettl, A. Longitudinal Splitting of Boron Nitride Nanotubes for the Facile Synthesis of High Quality Boron Nitride Nanoribbons. *Nano Lett.* **2011**, *11*, 3221–3226.
 - Li, L.; Li, L. H.; Chen, Y.; Dai, X. J.; Lamb, P. R.; Cheng, B.-M.; Lin, M.-Y.; Liu, X. High-Quality Boron Nitride Nanoribbons: Unzipping During Nanotube Synthesis. *Angew. Chem., Int. Ed.* **2013**, *52*, 4212–4216.
 - Molitor, F.; Güttinger, J.; Stampfer, C.; Graf, D.; Ihn, T.; Ensslin, K. Local Gating of a Graphene Hall Bar by Graphene Side Gates. *Phys. Rev. B* **2007**, *76*, 245426.
 - Tian, J. F.; Jauregui, L. A.; Lopez, G.; Cao, H.; Chen, Y. P. Ambipolar Graphene Field Effect Transistors by Local Metal Side Gates. *Appl. Phys. Lett.* **2010**, *96*, 093504.
 - Hähnlein, B.; Händel, B.; Pezoldt, J.; Töpfer, H.; Granzner, R.; Schwierz, F. Side-Gate Graphene Field-Effect Transistors with High Transconductance. *Appl. Phys. Lett.* **2012**, *101*.
 - Nouchi, R.; Saito, T.; Tanigaki, K. Determination of Carrier Type Doped from Metal Contacts to Graphene by Channel-Length-Dependent Shift of Charge Neutrality Points. *Appl. Phys. Express* **2011**, *4*, 035101.
 - Han, G. H.; Günes, F.; Bae, J. J.; Kim, E. S.; Chae, S. J.; Shin, H.-J.; Choi, J.-Y.; Pribat, D.; Lee, Y. H. Influence of Copper Morphology in Forming Nucleation Seeds for Graphene Growth. *Nano Lett.* **2011**, *11*, 4144–4148.
 - Luo, Z.; Lu, Y.; Singer, D. W.; Berck, M. E.; Somers, L. A.; Goldsmith, B. R.; Johnson, A. T. C. Effect of Substrate Roughness and Feedstock Concentration on Growth of Wafer-Scale Graphene at Atmospheric Pressure. *Chem. Mater.* **2011**, *23*, 1441–1447.
 - Giannozzi, P.; Baroni, S.; Bonini, N.; Calandra, M.; Car, R.; Cavazzoni, C.; Ceresoli, D.; Chiarotti, G. L.; Cococcioni, M.; Dabo, I.; et al. Quantum Espresso: A Modular and

- Open-Source Software Project for Quantum Simulations of Materials. *J. Phys.: Condens. Matter* **2009**, *21*, 395502.
45. Perdew, J. P.; Burke, K.; Ernzerhof, M., Generalized Gradient Approximation Made Simple. *Phys. Rev. Lett.* **1996**, *77*.
 46. Rappe, A. M.; Rabe, K. M.; Kaxiras, E.; Joannopoulos, J. D. Optimized Pseudopotentials. *Phys. Rev. B* **1990**, *41*, 1227–1230.
 47. Ramer, N. J.; Rappe, A. M. Designed Nonlocal Pseudopotentials for Enhanced Transferability. *Phys. Rev. B* **1999**, *59*, 12471.
 48. Monkhorst, H. J.; Pack, J. D. Special Points for Brillouin-Zone Integrations. *Phys. Rev. B* **1976**, *13*, 5188–5192.